Journal of
Mechanics of Materials and Structures

FERROMAGNETIC SHAPE MEMORY EFFECTS IN AN IRON PALLADIUM ALLOY

Jun Cui and Tom Shield

Volume 2, Nº 3 *March 2007*

mathematical sciences publishers

JOURNAL OF MECHANICS OF MATERIALS AND STRUCTURES
Vol. 2, No. 3, 2007

FERROMAGNETIC SHAPE MEMORY EFFECTS IN AN IRON PALLADIUM ALLOY

JUN CUI AND TOM SHIELD

This paper presents the results of an extensive series of experiments conducted on $Fe_{70}Pd_{30}$ using a recently developed apparatus, the Magneto-Mechanical Testing Machine. These experiments were designed to investigate the ferromagnetic shape-memory behavior of $Fe_{70}Pd_{30}$ and test the predictions of a theory that assumes the magnetizations of the material are constrained to lie in the easy directions and the material strains are constrained to be the shape-memory transformation strains. It was found that a specimen made of $Fe_{70}Pd_{30}$ single crystal lengthens when a magnetic field is applied along its c axis (short axis of FCT lattice) while the specimen is under uniaxial compression in the c direction. This behavior agrees with the predictions of the constrained theory and magnetic anisotropy measurements. The maximum field-induced strain change measured in this material is about 0.009 at 5500 G and -1 MPa, which is one fifth of the theoretical prediction. This is attributed to the magnetization rotation away from the easy directions caused by insufficient magnetic anisotropy. Under -12 MPa of compression the field-induced strain change is considerably smaller reaching only about 0.0008, but this change gives the largest work output observed of 9.6×10^3 J/m^3. This work output is very close to the work output of Terfenol-D under this amount of compressive stress.

1. Introduction

Shape memory alloys (SMAs) are materials that undergo a reversible, diffusionless structural transformation. At temperatures above the transformation temperature, these materials typically have a cubic crystal structure which is called the austenite phase. Below this transformation temperature the material structure has less symmetry in what is called the martensite phase. This reduction in symmetry gives rise to the formation of variants of the martensitic phase. The variants are related by the symmetry of the parent austenitic phase and in the absence of biasing stress all have the same free energy. If the SMA is also ferromagnetic (an FSMA) then there exists the possibility of rearranging the martensite variants using a magnetic field. Such a rearrangement can give changes in shape that involve strains one order of magnitude larger than those possible in "giant" magnetostrictive materials such as Terfenol-D.

Rearranging martensite variants by a magnetic field is a novel idea and has received considerable attention recently. The concept of combining martensitic phase transformation with magnetic field was first introduced by James and Kinderlehrer [1993]. Vasil'ev et al. [1996] measured the magnetostriction in $\langle 110 \rangle$ directions of a specimen made of Ni_2MnGa single crystal, and suggested the existence of field-induced shape memory effect. Ullakko et al. [1996] demonstrated field-induced variant rearrangement involving a 0.002 strain in unstressed Ni_2MnGa single crystal. In 1998, a larger reversible field-induced strain of 0.006 under cyclic fields of 10 kG has been achieved in $Fe_{70}Pd_{30}$ [James and Wuttig 1998].

Keywords: ferromagnetic shape memory, FePd, iron-palladium alloy.

Tickle et al. [1999] reported a field-induced strain of 0.045 in Ni_2MnGa. In their experiments, the movement of twin interfaces was directly observed verifying the basic FSMA mechanism. More recently, a field-induced strain of 0.094 was demonstrated by Sozinov et al. [2002]. Theories of field induced variant rearrangement have been developed in [James and Wuttig 1998; DeSimone and James 2002; O'Handley 1998]. According to the theory of James, Desimone, and Wuttig, if the magneto-crystalline anisotropy and elastic moduli of the material are large relative to the applied stress and magnetic fields, the strain-magnetization pair, $(\mathbf{E}(\mathbf{x}), \mathbf{m}(\mathbf{x}))$, can be reasonably assumed to only take the values at local energy minima (bottoms of the energy wells). In this case the free energy is reduced to only involving loading device and demagnetization terms and the minimization process becomes a process of determining the compatible microstructure and domain patterns that minimize this energy. From the solution to this constrained energy minimization problem, the microstructures and shape change of the material can be predicted as a function of the applied stress and magnetic fields. This constrained theory was applied to $Fe_{70}Pd_{30}$ [James and Wuttig 1998] and Ni_2MnGa [Tickle et al. 1999], and qualitative agreement between the theory and the experimental results was achieved. O'Handley [1998] approached the problem phenomenologically. He proposed a model for the magnetization process and field-induced twin boundary motion. His model includes an energy contribution associated with moving a twin interface and provides a simple explanation for the nearly linear field dependence of strain on magnetic field below saturation.

To date, Ni_2MnGa and $Fe_{70}Pd_{30}$ are the only two alloys reported exhibiting giant (>0.005) field-induced strain. The alloy Ni_2MnGa has received considerable attention recently, while $Fe_{70}Pd_{30}$ has attracted less attention. While the martensitic behavior of $Fe_{70}Pd_{30}$ had been previously studied extensively [Somura and Oshima and Fujita 1980; Oshima 1981; Oshima and Sugiyama 1982; Sugiyama et al. 1984; 1985; 1986; Muto et al. 1988; Oshima et al. 1988; 1990; Muto et al. 1990a; 1990b; 1990c; Tanaka and Oshima 1991; Oshima et al. 1992; Tanaka et al. 1992], only recently has the FSM behavior of this alloy been investigated [Cui and James 2001; Cui et al. 2004]. It was found that the FCC-FCT transformation in $Fe_{70}Pd_{30}$ is a weak first order thermoelastic transition. The average lattice parameters are $a = 3.822 \pm 0.001$ Å and $c = 3.629 \pm 0.001$ Å for the FCT martensite, and $a_0 = 3.755 \pm 0.001$ Å for the cubic austenite. The latent heat is 10.79 ± 0.01 J/cm^3. The Curie temperature is 450°C. The saturation magnetization is 1220 ± 10 emu/cm^3 for the martensite and 1080 ± 10 emu/cm^3 for the austenite; the easy axis is in [100] or [010] direction (a axes of FCT lattice). The magnetic anisotropy is $-5 \pm 2 \times 10^3$ erg/cm^3 for the austenite at 60°C, and $3.46 \pm 0.02 \times 10^5$ erg/cm^3 for the martensite at -20°C.

In this paper, a brief summary of the constrained theory is given, followed by the results of a series of magneto-mechanical tests. A comparison of the predictions of constrained theory with the results of these experiments is made and finally some conclusions are drawn.

2. Constrained theory

Constrained theory [DeSimone and James 2002] restricts the range of possible strain-magnetization pairs to those values that give absolute minima in the strain and anisotropy energies. This considerably reduces the complexity of the problem of predicting the microstructures and domain patterns that will form. In this section this theory and the process of solving problems using it will be summarized.

2.1. ***Constrained free energy.*** The free energy for a ferromagnetic shape memory material can be written as

$$F = \int_\Omega \{\phi(\mathbf{F}, \mathbf{m}, \theta) - \mathbf{h_0} \cdot \mathbf{m} - \sigma_\mathbf{0} \cdot \mathbf{E}\} d\mathbf{x} + \frac{1}{8\pi} \int_{\mathbb{R}^3} | \nabla \zeta_\mathrm{m} |^2 \, d\mathrm{x},$$

where Ω is the region occupied by the material in the reference configuration. The first term, $\phi(\mathbf{F}, \mathbf{m}, \theta)$, combines the strain and magnetic anisotropy energies and depends on the deformation gradient $\mathbf{F}$, magnetization $\mathbf{m}$, and temperature θ. The applied magnetic field is $\mathbf{h}_0$, the applied stress is σ_0, and the strain is $\mathbf{E}$. The second integral is the demagnetization energy, where the magnetostatic potential ζ_m is obtained by solving the magnetostatic equation

$$\mathrm{div}(-\nabla \zeta_\mathrm{m} + 4\pi \mathbf{m}) = 0,$$

which itself follows from Maxwell's equations,

$$\begin{aligned} &\mathrm{curl}\, \mathbf{h} = 0 \ (\mathbf{h} = -\nabla \zeta_\mathrm{m}), \\ &\mathrm{div}(\mathbf{h} + \mathbf{4}\pi \mathbf{m}) = 0. \end{aligned}$$

According to the constrained theory of DeSimone and James [2002], if the magnetic anisotropy and elastic moduli of the material are large compared to the applied stress and magnetic field, the strain-magnetization pair $(\mathbf{E}(\mathbf{x}), \mathbf{m}(\mathbf{x}))$ will be close to the energy wells, which are given by

$$\phi(\mathbf{F}, \mathbf{m}, \theta) = 0. \tag{1}$$

Assuming the solution is constrained to be exactly on bottom of these energy wells, the constrained free energy is then given by

$$\int_\Omega \{-\mathbf{h_0} \cdot \mathbf{m} - \sigma_\mathbf{0} \cdot \mathbf{E}\} d\mathbf{x} + \frac{1}{8\pi} \int_{\mathrm{R}^3} | \nabla \zeta_\mathrm{m} |^2 \, d\mathbf{x}. \tag{2}$$

2.2. ***Average microstructural behavior.*** If the magnetization-strain states are combined to form a compatible microstructure and it is assumed that this microstructure consists of very fine twins, then the problem can be further relaxed (in the terminology of [DeSimone and James 2002]) and only the average values of the strain and magnetization need be considered. These average values lie in the convex hull of the energy wells, $\mathscr{C}$, which is defined as follows. The alloy $Fe_{70}Pd_{30}$ has three tetragonal variants and each variant has a strain and two easy directions that satisfy (1) (at a fixed temperature). Thus the constrained theory strain-magnetization pairs for this alloy are

$$\begin{aligned} \mathbf{E}_1 &= \begin{pmatrix} \epsilon_2 & 0 & 0 \\ 0 & \epsilon_1 & 0 \\ 0 & 0 & \epsilon_1 \end{pmatrix} \text{ and any of } \begin{matrix} \pm[\mathbf{m}_1^2 = m_\mathrm{s}\mathbf{e}_2], \\ \pm[\mathbf{m}_1^3 = m_\mathrm{s}\mathbf{e}_3], \end{matrix} \\ \mathbf{E}_2 &= \begin{pmatrix} \epsilon_1 & 0 & 0 \\ 0 & \epsilon_2 & 0 \\ 0 & 0 & \epsilon_1 \end{pmatrix} \text{ and any of } \begin{matrix} \pm[\mathbf{m}_2^1 = m_\mathrm{s}\mathbf{e}_1], \\ \pm[\mathbf{m}_2^3 = m_\mathrm{s}\mathbf{e}_3], \end{matrix} \\ \mathbf{E}_3 &= \begin{pmatrix} \epsilon_1 & 0 & 0 \\ 0 & \epsilon_1 & 0 \\ 0 & 0 & \epsilon_2 \end{pmatrix} \text{ and any of } \begin{matrix} \pm[\mathbf{m}_3^1 = m_\mathrm{s}\mathbf{e}_1], \\ \pm[\mathbf{m}_3^2 = m_\mathrm{s}\mathbf{e}_2], \end{matrix} \end{aligned} \tag{3}$$

where $\epsilon_1 = a/a_0 - 1$ and $\epsilon_2 = c/a_0 - 1$ are the transformation strains and m_s is the saturation magnetization of the martensite. The strain tensor and magnetization vector components are in the cubic crystallographic coordinates of the parent austenite phase, which has basis vectors $\mathbf{e}_k$, $k = 1, 2, 3$.

The set $\mathcal{C}$, which is comprised of average strain, $\langle \mathbf{E} \rangle$, and average magnetization, $\langle \mathbf{m} \rangle$, pairs, is given by a sum of the combinations in (3); thus $(\langle \mathbf{E} \rangle, \langle \mathbf{m} \rangle)$ lies in $\mathcal{C}$ if and only if two conditions are satisfied:

$$\begin{aligned} \langle \mathbf{m} \rangle &= \lambda_1 \mathbf{m}_1^2 + \lambda_2(-\mathbf{m}_1^2) + \lambda_3 \mathbf{m}_1^3 + \lambda_4(-\mathbf{m}_1^3) + \lambda_5 \mathbf{m}_2^1 + \lambda_6(-\mathbf{m}_2^1) \\ &\quad + \lambda_7 \mathbf{m}_2^3 + \lambda_8(-\mathbf{m}_2^3) + \lambda_9 \mathbf{m}_3^1 + \lambda_{10}(-\mathbf{m}_3^1) + \lambda_{11} \mathbf{m}_3^2 + \lambda_{12}(-\mathbf{m}_3^2), \\ \langle \mathbf{E} \rangle &= (\lambda_1 + \lambda_2 + \lambda_3 + \lambda_4)\mathbf{E}_1 + (\lambda_5 + \lambda_6 + \lambda_7 + \lambda_8)\mathbf{E}_2 + (\lambda_9 + \lambda_{10} + \lambda_{11} + \lambda_{12})\mathbf{E}_3, \end{aligned} \tag{4}$$

where λ_i, $i = 1 \ldots 12$ are the volume fractions of the domains inside the variants that have magnetizations $\pm \mathbf{m}_j^k$ and strains $\mathbf{E}_i$ in the combinations given in (3). The volume fractions are subject to the constraints

$$\sum_{i=1}^{12} \lambda_i = 1, \quad 0 \le \lambda_i \le 1, \ i = 1 \ldots 12. \tag{5}$$

Figure 1 presents a geometrical interpretation of the convex hull.

Equation (4) can be simplified as follows. Let $\xi_j = \lambda_{2j-1} + \lambda_{2j}$ and $\eta_j = \lambda_{2j-1} - \lambda_{2j}$, where $j = 1 \ldots 6$. Then note that $\xi_1 + \xi_2$, $\xi_3 + \xi_4$ and $\xi_5 + \xi_6$ are the volume fractions of variants $\mathbf{E}_1$, $\mathbf{E}_2$ and $\mathbf{E}_3$ and $\eta_1 + \eta_2$, $\eta_3 + \eta_4$ and $\eta_5 + \eta_6$ are the net magnetization associated with these strains, respectively. The average magnetization in (4) then reduces to

$$\langle \mathbf{m} \rangle = \eta_1 \mathbf{m}_1^2 + \eta_2 \mathbf{m}_1^3 + \eta_3 \mathbf{m}_2^1 + \eta_4 \mathbf{m}_2^3 + \eta_5 \mathbf{m}_3^1 + \eta_6 \mathbf{m}_3^2,$$

which for the specific forms of $\mathbf{m}_j^k$ in (3) has components

$$\langle \mathbf{m} \rangle = m_s \begin{pmatrix} \eta_3 + \eta_5 \\ \eta_1 + \eta_6 \\ \eta_2 + \eta_4 \end{pmatrix}.$$

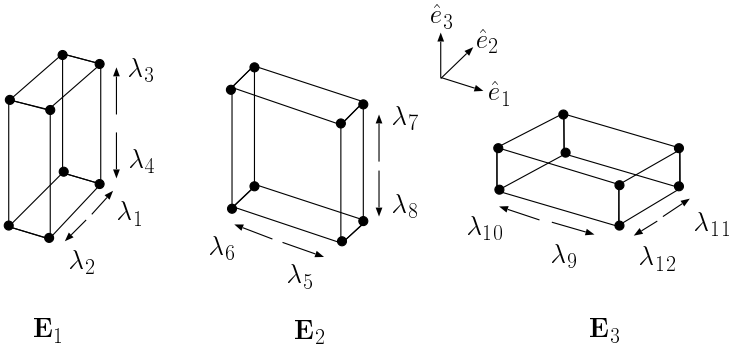

Figure 1. Schematic drawing of an FCT lattice and its three possible variants is shown. The tetragonality of the lattice is exaggerated. The arrows labeled with $\lambda_{1\ldots12}$ are the possible magnetization directions (easy axes) for each variant in the constrained theory.

The average strain defined in (4) also reduces to

$$\langle \mathbf{E} \rangle = (\xi_1 + \xi_2)\mathbf{E}_1 + (\xi_3 + \xi_4)\mathbf{E}_2 + (\xi_5 + \xi_6)\mathbf{E}_3, \tag{6}$$

where the nonzero components of $\langle \mathbf{E} \rangle$ are

$$\begin{aligned}
\langle \mathbf{E} \rangle_{11} &= (\xi_1 + \xi_2)\epsilon_2 + (\xi_3 + \xi_4 + \xi_5 + \xi_6)\epsilon_1, \\
\langle \mathbf{E} \rangle_{22} &= (\xi_3 + \xi_4)\epsilon_2 + (\xi_1 + \xi_2 + \xi_5 + \xi_6)\epsilon_1, \\
\langle \mathbf{E} \rangle_{33} &= (\xi_5 + \xi_6)\epsilon_2 + (\xi_1 + \xi_2 + \xi_3 + \xi_4)\epsilon_1,
\end{aligned}$$

using the forms of $\mathbf{E}_i$ in (3). The constraints (5) in terms of ξ_j and η_j are

$$\sum_{j=1}^{6} \xi_j = 1, \quad 1 \geq \xi_j \geq |\eta_j|, \ j = 1 \ldots 6.$$

In the limit as the microstructure becomes infinitely fine the demagnetization energy can be calculated using the results for a uniformly magnetized body [DeSimone and James 2002], which is $\frac{1}{2}\langle \mathbf{m} \rangle \cdot \mathbf{D}\langle \mathbf{m} \rangle$, where $\mathbf{D}$ is the magnetometric demagnetization matrix for the specimen geometry. Then the constrained free energy (2) reduces to

$$-\mathbf{h_0} \cdot \langle \mathbf{m} \rangle - \sigma_\mathbf{0} \cdot \langle \mathbf{E} \rangle + \tfrac{1}{2}\langle \mathbf{m} \rangle \cdot \mathbf{D}\langle \mathbf{m} \rangle,$$

which is to be minimized over $(\langle \mathbf{E} \rangle, \langle \mathbf{m} \rangle) \in \mathscr{C}$. This is an exact result if the specimen has an ellipsoidal shape and an approximation for any other geometry.

For the case of a rectangular specimen with a square base and a height in the x_1 direction which is much longer than the two other dimensions, the demagnetization matrix can be approximated by the demagnetization matrix of an infinitely long cylinder, $\mathbf{D} = \mathrm{diag}(0, 2\pi, 2\pi)$. If the applied field is restricted to the (x_1, x_2) plane and the applied stress is uniaxial in the x_1 direction with magnitude σ, then the constrained free energy, $\mathscr{E}$, becomes

$$\mathscr{E} = -h_1 m_s(\eta_3 + \eta_5) - h_2 m_s(\eta_1 + \eta_6) + \pi m_s^2 \left((\eta_1 + \eta_6)^2 + (\eta_2 + \eta_4)^2\right) - \sigma\,(\xi_3 + \xi_4 + \xi_5 + \xi_6)(\epsilon_1 - \epsilon_2) - \sigma\epsilon_2. \tag{7}$$

2.3. ***Energy minimization.*** Finding the minimizers of the constrained free energy given by Equation (7) can be broken into two steps: First, a minimization over ξ_j, $j = 1 \ldots 6$, is performed using linear programming. In the second step the energy is minimized with respect to the remaining variables, η_j, $j = 1 \ldots 6$.

Figure 2 and Table 1 summarize results of this process for a magnetic field with $h_1 \geq 0$ and $h_2 \geq 0$ combined with a uniaxial stress, $\sigma \leq 0$. As shown on this figure, the solution can be divided into four distinct regions, which involve three possible microstructures. In region A, only martensite variant $\mathbf{E}_1$ is present, and its net magnetization is given by $\eta_1 m_s \mathbf{e}_2$ which depends on the magnitude and direction of magnetic field h_2. In region D, martensite variants $\mathbf{E}_2$ and $\mathbf{E}_3$ may coexist. Their net magnetizations are $\eta_3 m_s \mathbf{e}_1$ and $\eta_5 m_s \mathbf{e}_1$, respectively. In the remaining regions, B and C, all three variants may be present. The admissible microstructures that these variants may form in each of these solution regions are discussed next.

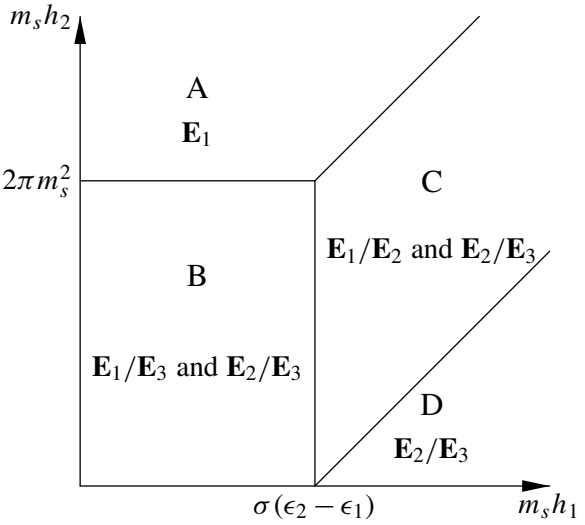

Figure 2. Summary of the minimum energy solution for $h_1 \geq 0$, $h_2 \geq 0$ with constant applied stress $\sigma < 0$, is shown. The volume fraction values for the areas labeled A–D are given in Table 1. The pairs of strains listed in each region are those that minimize the energy and are magnetically compatible across one or both of their possible twin interfaces.

Table 1 shows the results of the energy minimization for the variables η_j only. This is because the variables ξ_j cannot be always fully determined. For example, in region A energy minimization gives $\eta_1(=\lambda_1-\lambda_2)=1$, and because of the constraint $\lambda_i \leq 1$, $i = 1 \ldots 12$, the solution is $\lambda_1 = 1$ and $\lambda_i = 0$, $i = 2 \ldots 12$ and the ξ_j are fully determined. In region C, energy minimization gives 5 equations and 3 inequalities, plus the constraints. Many combinations of the λ_i satisfy these conditions, so ξ_j cannot be determined. However, without knowing the values of ξ_j, the overall strain of the specimen can still

Area	η_1	η_3	η_5	$\mathscr{E}$
A	1	0	0	$-h_2 m_s + \pi m_s^2 - \lvert\sigma\rvert\epsilon_2$
B	$\dfrac{h_2}{2\pi m_s}$	0	0	$-\dfrac{h_2^2}{4\pi} - \lvert\sigma\rvert\epsilon_2$
C	$\dfrac{(h_2-h_1)m_s - \lvert\sigma\rvert(\epsilon_1-\epsilon_2)}{2\pi m_s^2}$ $0 <, \ < 1$	$1-\eta_1-\eta_5$ ≥ 0	≥ 0	$-\dfrac{\left((h_2-h_1)m_s - \lvert\sigma\rvert(\epsilon_1-\epsilon_2)\right)^2}{4\pi m_s^2}$ $-h_1 m_s - \lvert\sigma\rvert\epsilon_1$
D	0	$1-\eta_5$	≥ 0	$-h_1 m_s + \lvert\sigma\rvert\epsilon_1$

Table 1. Values for the areas A–D of Figure 2. For all areas shown, $\eta_2 = \eta_4 = \eta_6 = 0$.

	$\mathbf{E}_1/\mathbf{E}_2$	$\mathbf{E}_1/\mathbf{E}_3$	$\mathbf{E}_2/\mathbf{E}_3$
$\sqrt{2}\mathbf{a}/\gamma$	$[\bar{1}10]$ $[110]$	$[101]$ $[\bar{1}01]$	$[0\bar{1}1]$ $[011]$
$\sqrt{2}\hat{\mathbf{n}}$	$[\bar{1}\bar{1}0]$ $[1\bar{1}0]$	$[10\bar{1}]$ $[\bar{1}0\bar{1}]$	$[0\bar{1}\bar{1}]$ $[01\bar{1}]$

Table 2. Twin solutions from linear geometric martensite theory. The normal to the twin plane is $\hat{\mathbf{n}}$ and the shape strain is $\mathbf{a}$. Each pair of variants can form two different twins. The magnitude of the shape strain is $\gamma = |\epsilon_1 - \epsilon_2| = 0.0515$.

be evaluated. For example, in region D, both variants $\mathbf{E}_2$ and $\mathbf{E}_3$ can coexist, and it is not possible to fully determine the values λ_i. Nonetheless, the specimen can be determined to be at its maximum length because both variant $\mathbf{E}_2$ and $\mathbf{E}_3$ have their long axes aligned with the long axis of the specimen.

2.4. ***Magnetoelastic compatibility and energy minimizing microstructures.*** Without considering kinematic and magnetic compatibility, free energy minimization predicts three possible combinations of variants. However, some of these combinations may not be compatible and must be excluded as possible energy minimizing microstructures. The microstructures that are magnetoelastically compatible for $h_1 \geq 0$, and $h_2 \geq 0$ are discussed below. Microstructures in the other three quadrants can be found by symmetry.

If martensite variants $\mathbf{E}_i$ and $\mathbf{E}_j$ meet at a planar interface, linearized kinematic compatibility requires

$$\mathbf{E}_i - \mathbf{E}_j = \tfrac{1}{2}(\mathbf{a} \otimes \hat{\mathbf{n}} + \hat{\mathbf{n}} \otimes \mathbf{a}), \tag{8}$$

where the vector $\mathbf{a}$ is the shape strain and $\hat{\mathbf{n}}$ is the normal to the interface. Given a pair of variant strains, equation (8) can be solved for $\mathbf{a}$ and $\hat{\mathbf{n}}$. In the tetragonal case considered here, there are two solutions of (8) for each pair of variants, which gives a total of six possible twin interfaces in this material. These are listed in Table 2.

Once the twin interface is determined from kinematics, magnetic compatibility across this interface must also be satisfied. This requires that the jump in the normal component of the magnetization across the interface must be zero, that is,

$$(\mathbf{m}_i - \mathbf{m}_j) \cdot \hat{\mathbf{n}} = 0, \tag{9}$$

where $\mathbf{m}_i$ and $\mathbf{m}_j$ are net magnetization of variants $\mathbf{E}_i$ and $\mathbf{E}_j$, respectively. The minima presented in Figure 2 and Table 1 will next be checked that they satisfy (9) for interfaces between the predicted variants.

The solution in area A of Figure 2 involves only variant $\mathbf{E}_1$, thus there are no twin interfaces across which compatibility must be satisfied.

The microstructure in area D consists of variants $\mathbf{E}_2$ with a net magnetization of $\eta_3 m_s \mathbf{e}_1$, and $\mathbf{E}_3$ with a net magnetization of $\eta_5 m_s \mathbf{e}_1$. The two possible twin interfaces between these two variants have normals $[0\bar{1}\bar{1}]$ and $[01\bar{1}]$. The difference between these two magnetizations is $(\eta_3 - \eta_5) m_s \mathbf{e}_1$, which is perpendicular to both of these twin plane normals for any values of η_3 and η_5. Thus this microstructure is magnetically compatible.

Areas B and C may contain microstructures that involve all three variants. Possible combinations are $\mathbf{E}_1$ with $\mathbf{E}_2$, $\mathbf{E}_1$ with $\mathbf{E}_3$, and $\mathbf{E}_2$ with $\mathbf{E}_3$. The last case is the same as that for area D, and because it was found to be always magnetically compatible, both areas B and C may contain twins with variants $\mathbf{E}_2$ and $\mathbf{E}_3$. The other two possible twins will be considered in turn.

For the combination of $\mathbf{E}_1$ and $\mathbf{E}_2$, the possible interface normals between these two variants are $[\bar{1}\bar{1}0]$ and $[1\bar{1}0]$. From the results of energy minimization, the net magnetization within these two variants are $\eta_1 m_s \mathbf{e}_2$ and $\eta_3 m_s \mathbf{e}_1$, respectively. Their difference is $(-\eta_3, \eta_1, 0)$, which is perpendicular to the interface normal $[\bar{1}\bar{1}0]$ if $\eta_1 = \eta_3$ and perpendicular to $[1\bar{1}0]$ if $\eta_1 = -\eta_3$. Because both η_1 and η_3 are required to be positive by the minimization, the second interface is not possible in either area B or C. Area B minimization requires $\eta_3 = 0$; thus unless $h_2 = 0$, the remaining twin interface is not possible in area B. In area C, the requirement that $\eta_1 = \eta_3$ restricts $\eta_5 = 1 - 2\eta_1$, which is possible and thus so is this twin in area C.

For the combination of $\mathbf{E}_1$ and $\mathbf{E}_3$, the normals to the possible interfaces between these two variants are $[10\bar{1}]$ and $[\bar{1}0\bar{1}]$. Energy minimization determined the net magnetization within these two variants to be $\eta_1 m_s \mathbf{e}_2$ and $\eta_5 m_s \mathbf{e}_1$, respectively. Their difference is $(-\eta_5, \eta_1, 0)$, which is perpendicular to these interface normals only if $\eta_5 = 0$. This is already required by minimization in area B, thus this twin is allowed in this area. In area C, η_5 is nonzero in general and thus this twin is not allowed in this area.

Figure 2 summarizes the results of both energy minimization and the requirements of compatibility and it shows the valid twin combinations in each of the four regions. The applied loading, σ, is in the x_1 direction and the change in length of the material in this direction is of interest because it is the deformation that does work against the applied stress. In area A the normal strain in the x_1 direction is ϵ_2 which is less than one for this material. The microstructure in area D is a combination of variants that both have ϵ_1 as their normal strain in the x_1 direction. Thus selecting an applied field path that goes from area A to area D will result in a change in the x_1 direction normal strain of $\epsilon_1 - \epsilon_2 = (a - c)/a_0 = 0.0515$. The experiments discussed below were designed to test this prediction.

3. Equipment and sample preparation

Combined mechanical and magnetic tests were performed with a facility called the Magneto-Mechanical Test Machine (MMTM). Details of this machine can be found in [Shield 2003]. Two $Fe_{70}Pd_{30}$ single crystal specimens, MM6 and MM10, were used in the magneto-mechanical tests that are reported here. They were cut in close proximity to each other from the single crystal boule FePd4 (see [Cui et al. 2004] for more information regarding this boule). The composition of both specimens MM6 and MM10 is near 29.6 at.% Pd. Their martensitic/austenitic transformation temperatures are $M_s \approx 20°C$, $M_f \approx 16°C$, $A_s \approx 18°C$, and $A_f \approx 25°C$. Specimen MM6 has dimensions of $2.12 \times 2.10 \times 6.52$ mm^3, and specimen MM10 has dimensions of $2.11 \times 2.10 \times 8.65$ mm^3. Both specimens are rectangular bars with {100} surfaces. The long dimension of each specimen is used as the loading direction and will be called the longitudinal specimen direction. The transverse direction is perpendicular to the longitudinal direction and it is along a short specimen dimension. Their orientation was checked by x-ray diffractometry at 60°C. The surface normals vary by about 0.7° from ⟨100⟩ for MM6, and 0.5° for MM10. Both of them were polished at 70°C with 0.1 μm diamond suspension.

4. Test design

A series of tests with different temperatures, amounts of compressive stress and magnetic field paths are summarized in Table 3. This table lists twenty-five tests divided into four sets in the order they will be discussed below. For each test there are three groups of columns. Initially all tests start with the specimen at 35°C and at the conditions (stress and field) listed in the first group of columns. The specimen is then

Test	Start at 35°C Field (G)	Start at 35°C Stress (MPa)	Ferro. Strain Measurements Temp. (°C)	Ferro. Strain Measurements Stress (MPa)	Ferro. Strain Measurements Field Path(s)	End to 35°C Field (G)	End to 35°C Stress (MPa)
			Set 1				
T5,T10	0	−1.0	11	−1.0	Rot-9radii	0	−1.0
T6	0	−2.0	11	−2.0	Rot-9radii	0	−2.0
T7	0	−4.0	11	−4.0	Rot-9radii	0	−4.0
T11	0	−6.0	11	−6.0	Rot-9radii	0	−6.0
T8	0	−8.0	11	−8.0	Rot-9radii	0	−8.0
T9	0	−12.0	11	−12.0	Rot-9radii	0	−12.0
			Set 2				
T13b	0	−1.0	20	−1.0	Rot2-5515	0	−1.0
T13c	0	−1.0	15	−1.0	Rot2-5515	0	−1.0
T13d	0	−1.0	10	−1.0	Rot2-5515	0	−1.0
T14a	0	−1.0	5	−1.0	Rot2-5515	0	−1.0
T14b	0	−1.0	0	−1.0	Rot2-5515	0	−1.0
T14c	0	−1.0	−5	−1.0	Rot2-5515	0	−1.0
			Set 3				
T12,T15	0	−12.0	11	−1.0	Rot20-5515	0	−1.0
T16	0	−1.0	11	−1.0	Rot20-5515	0	−1.0
T17	0	−1.0	11	−1.0	Rot20-3818	0	−1.0
			Set 4				
T2	0	0	11	−2.0	Lin-4242, Arc-4242		
			11	−1.0	Lin-4242, Arc-4242	0	−1.0
T3	0	−2.0	11	−2.0	Lin-4242, Arc-4242		
			11	−2.0	Rot1-4242		
			11	−1.0	Lin-4242, Arc-4242		
			11	−1.0	Rot1-4242	0	−1.0
T4	T4242	−2.0	11	−2.0	Lin-4242, Arc-4242		
			11	−2.0	Rot1-4242		
			11	−1.0	Lin-4242, Arc-4242		
			11	−1.0	Rot1-4242	0	−1.0

Table 3. Tests conducted on specimens MM6 and MM10. Terms such as T4242, Lin-4242, Arc-4242, and so on are explained in Section 4.

cooled, at approximately 1°C/min to the temperature listed in the second group of columns. The second group of columns includes three columns. The first two are the temperature and the bias stress at which the measurements conducted and the third column describes the path(s) of the magnetic field applied during the test. After the applied magnetic field path(s) have been completed, the specimen temperature

is raised back up to 35°C under the conditions listed in the last group of columns. Tests in Set 1 have two different sets of field paths that were performed under two different amounts of compressive stress. By starting all tests at 35°C, which is above the austenite finish temperature, all martensitic microstructure is removed from the specimen. This makes sure each test starts from identical and repeatable conditions.

In Table 3 the magnetic field conditions and paths are specified with labels. For the only field applied during cooling, the label T4242 indicates a field applied along the transverse direction of the specimen [100] at a magnitude of 4242 G. There are two basic field paths applied to the specimen to measure its FSM response. Linear paths follow radial lines that start or end at zero field. Rotation or arc paths follow circles or parts of circles, which keep the magnitude of the applied field constant and change its direction. Field path Lin-4242 consists of two segments: first, the magnetic field is applied on the transverse direction of the specimen [100] from 0.0 G to 4242 G, then back to 0.0 G along the same direction; second, it increases on the longitudinal [001] direction from 0.0 G to 4242 G, and returns back to 0.0 G on [001] axis. For the Arc-4242 path, the field first increases along the transverse [100] direction from 0.0 G to 4242 G, then rotates 90° counterclockwise (CCW) toward the longitudinal [001] direction with constant magnitude. Once the rotation is complete, the field decreases from 4242 G to 0.0 G along longitudinal direction. The field rate is 60 G/sec on all segments of both Lin-4242 and Arc-4242 paths. These two paths were designed to investigate the path dependence of the FSM effect, as they both include the points at 4242 G in both the transverse and then the longitudinal directions.

The path Rot-9radii has nine circular segments. It starts by increasing the field in transverse [100] direction from zero to 424 G at a rate of 60 G/sec, the field is then rotated 360° CCW at a rate of 6 G/sec, the first segment finishes when the field returns to 424 G in the transverse direction. The second segment starts at the end of the first segment, the field increases in the transverse direction from 424 G to a new magnitude, 848 G, at a rate of 12 G/sec. It then rotates 360° CCW at a rate of 12 G/sec, and finishes by returning to 848 G in the transverse direction. The next seven segments are similar to the two segments described above with larger field magnitudes. Finally the field is decreased back to 0.0 G while pointing in the transverse direction. The radii of the nine circles are 424, 848, 1273, 1697, 2121, 2969, 3818, 4666, and 5515 G, which are completed at field rates of 6, 12, 18, 24, 30, 42, 54, 66, and 78 G/sec, respectively. These rates result in each 360° circle being completed in 444 seconds.

The path Rot1-4242 consists of a single circle. The field first increases in the transverse [001] direction of the specimen from 0.0 G to 4242 G. Then the field rotates 360° CCW with constant magnitude. After the rotation is complete the field decreases from 4242 G to 0.0 G while pointing in the transverse direction. The field rate is 60 G/sec for the entire path. Paths Rot2-5515 and Rot20-5515 are similar paths that repeat the same circular path twice and twenty times, respectively. In both paths the magnetic field is first applied in the transverse [100] direction of the specimen and increased from 0.0 G to 5515 G. Then the field rotates 720° and 7200° CCW, respectively. After the rotations are complete, the field then decreases from 5515 G to 0.0 G while pointing in the transverse direction. The field rates are 60 G/sec for the linear segments, and 78 G/sec for the circles. The field path Rot20-3818 is similar to the path Rot20-5515, except that the magnitude of the field is 3818 G with a rate of 54 G/sec.

Tests T5 to T10 were designed to study work output, but they also provide information on the effects of stress on phase transformation temperatures. However, due to the limitation of the space, phase transformation effects will be discussed in another paper, along with some other tests which were designed to study the effect of magnetic field on phase transformation temperature [Cui et al. $\geq$ 2008].

5. Experimental results

We now give the results of the experiments and compare them to the constrained theory presented above.

5.1. ***Ferromagnetic strain, blocking stress and work output.*** The key property of interest for FSMAs is the field-induced (or ferromagnetic) strain amplitude, which is defined as the amplitude of the strain change in the specimen caused by an application of a cyclic magnetic field holding stress and temperature constant. In many materials, when the stress exceeds a critical level there will be no ferromagnetic strain no matter how large the applied magnetic field is, and this critical stress is called the blocking stress. Another important property is the work output, which is defined as the product of the ferromagnetic strain amplitude and the constant stress at which this ferromagnetic strain is achieved.

The tests listed in set 1 of Table 3 were designed to give a complete picture of the ferromagnetic strain amplitudes achievable in $Fe_{70}Pd_{30}$ over a wide range of applied field magnitudes and compressive stresses. In Figure 3, the applied magnetic field and the strain are plotted verses time for tests T6 to T11.

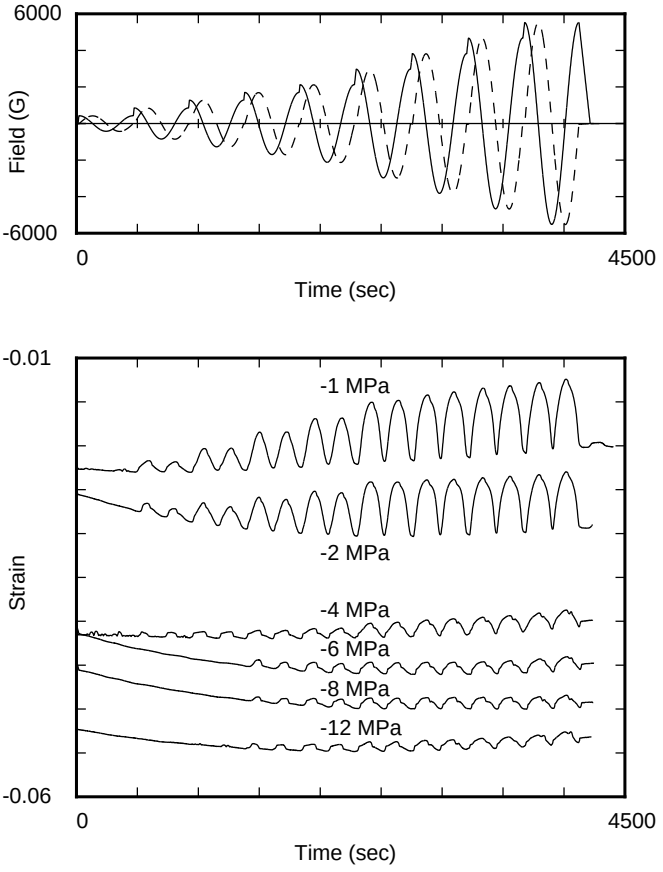

Figure 3. Top: A time history of the applied magnetic fields for field path Rot-9radii. Solid curve is the transverse component of field, and dashed curve is the longitudinal component. Bottom: Time history of the strains measured in tests T5-T9 on specimen MM6 at 11°C.

Because a 180° change in field direction results in a complete ferromagnetic strain cycle, the measured strain goes through two cycles for every 360° of field rotation. The figure shows that the amplitude of the ferromagnetic strain decreases with increasing compressive stress and increases with increasing magnetic field amplitude. The strain at −1 MPa started to oscillate in response to the field after the amplitude of the field exceeded about 800 G; the amplitude of the ferromagnetic strain then increased rapidly with increasing field amplitude until the field reached approximately 3000 G. After this point, the strain amplitude only increased slightly with further increases in the field. The −2 MPa curve is similar to the −1 MPa curve with slightly smaller ferromagnetic strain. The −4 MPa curve has a much smaller strain amplitude than the lower stress curves and the specimen starts to respond to the field at smaller value, 424 G. The −6 MPa curve was significantly different from the −1, −2, and −4 MPa curves because it does not oscillate until the field exceeds 1700 G. The −8 and −12 MPa curves are similar to the −6 MPa curve except that the field-induced strains are even smaller.

Table 4 and Figure 4 summarize the field-induced strain amplitude and work output at various stress levels for both specimens. Figure 4 also includes data on Terfenol-D [Clark 1980] and Ni_2MnGa [Tickle and James 1999] for comparison. The ferromagnetic strain amplitude was calculated using the maximum and minimum strain within a single strain cycle due to the largest magnetic field. The ferromagnetic strain amplitude decreases quickly with increasing compressive stress. After −4 MPa, the rate of decrease slows and it is not clear at what stress level the amplitude will decrease to zero. This unusual behavior seems to indicate that there is no blocking stress for this material or that there is a combination of effects active at the same time. In fact, both specimens still responded to field even at −12 MPa. At this level, the field-induced strain and work output of MM10 is similar to that of Terfenol-D, and is larger than that of Ni_2MnGa. Figure 4 shows that Ni_2MnGa has a higher strain at smaller stresses, but stops responding to magnetic field after −8 MPa. Terfenol-D on the other hand stays active beyond −50 MPa, and its largest work output occurs near −20 MPa. The strain available in Terfenol-D is far less than Ni_2MnGa at low stress levels. The behavior of $Fe_{70}Pd_{30}$ is in between these two materials. Compared to Ni_2MnGa, $Fe_{70}Pd_{30}$ has less strain at small stresses and more strain at higher stress levels. When $Fe_{70}Pd_{30}$ is compared to Terfenol-D, the situation is reversed. The behavior of $Fe_{70}Pd_{30}$ beyond −12 MPa could not

Stress (MPa)	Sample MM6 Strain	Sample MM6 Work output (J/m^3)	Sample MM10 Strain	Sample MM10 Work output (J/m^3)
−1	0.0084	8.4×10^3	0.0059	5.9×10^3
−2	0.0070	1.4×10^4	0.0042	8.4×10^3
−4	0.0025	1.0×10^4	0.0025	1.0×10^4
−6	0.0019	1.1×10^4	0.0016	9.8×10^3
−8	0.0016	1.3×10^4	0.0011	8.8×10^3
−12	0.0017	2.1×10^4	0.0008	9.6×10^3

Table 4. Ferromagnetic strain amplitude at various bias stresses and the corresponding work output. The MM6 strains are from the crosshead displacement, while the MM10 strains are from the capacitive sensor.

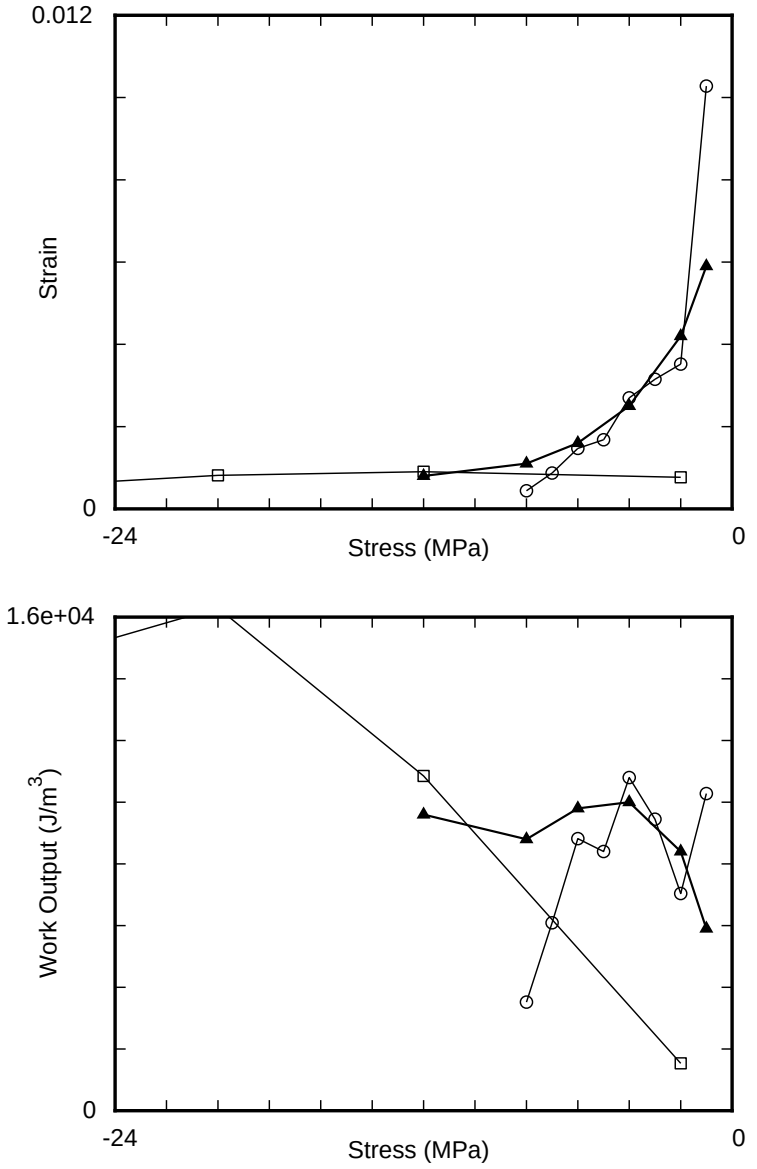

Figure 4. Strains induced by magnetic field at various load conditions and corresponding work output for $Fe_{70}Pd_{30}$ specimen MM10 (solid triangle), Ni_2MnGa (circle) [Tickle and James 1999], and Terfenol-D (square) [Clark 1980].

be determined because of the presence of the FCT to BCT transformation, which is not reversible. There is some evidence that the yield stress of $Fe_{70}Pd_{30}$ is higher than -20 MPa (possible slip bands appeared on one specimen that was overloaded).

The details of the strain induced by magnetic field at different levels of stress are provided in Figure 5, which gives the strain verses both the transverse and longitudinal components of applied field. Each

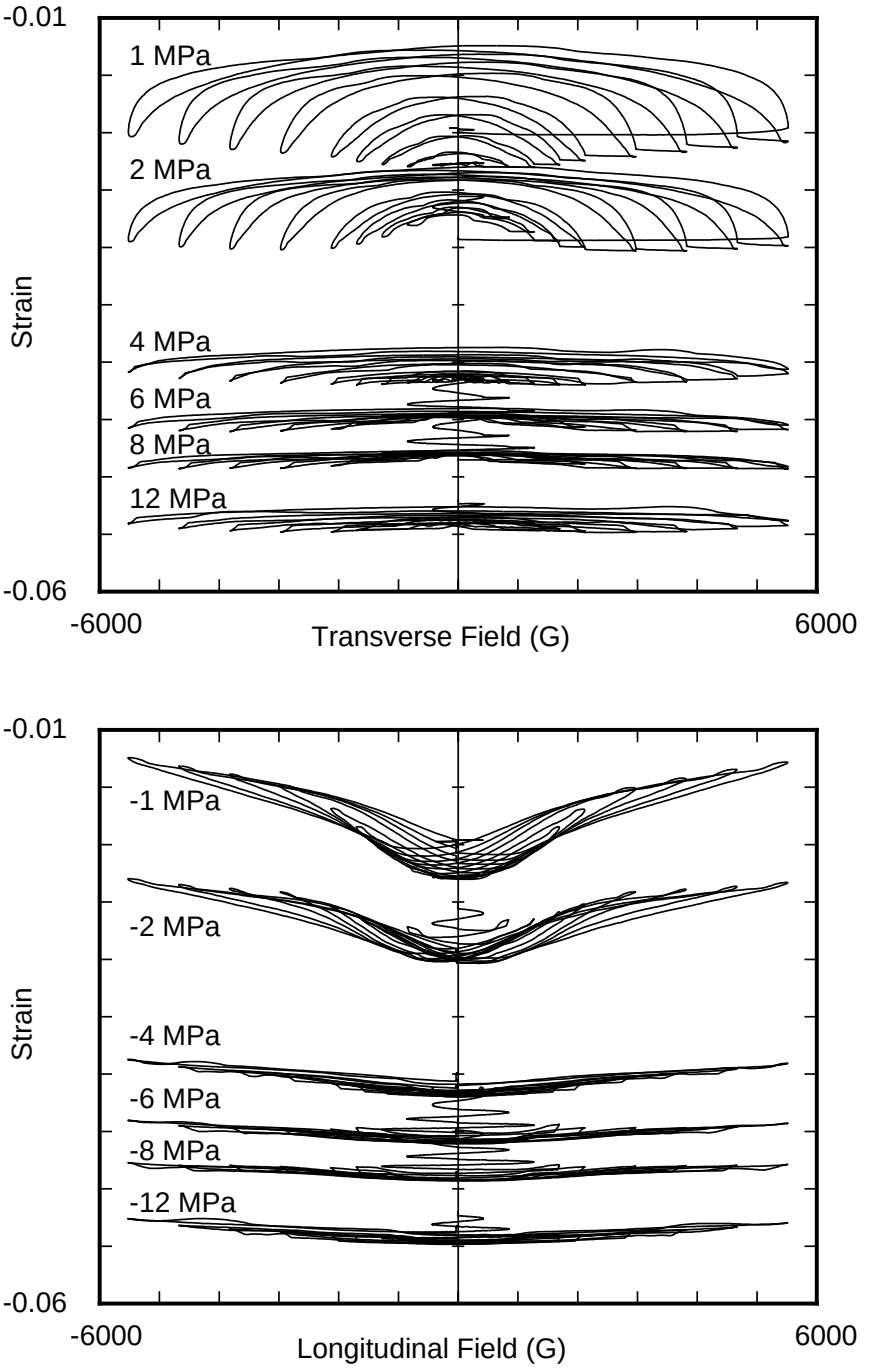

Figure 5. Ferromagnetic strains vs. transverse (top) and longitudinal (bottom) component of field at various load conditions for specimen MM6 are given. Each curve has the same magnetic field path (Rot-9radii) and temperature of 11°C.

set of curves at one load level includes data for all nine field levels in the path Rot-9radii. The curves at −1 MPa show that the changes in strain were small when the transverse component of the field was between −4500to 4500 G, and were substantial between 4500 to 5515 G and −4500 to −5515 G. If the curves are examined from the perspective of the longitudinal component of field, the changes of the strain were substantial between −1000 to 1000 G, and they were smaller over the rest of the range. This point is better illustrated by Figure 6, which shows the strain versus the angle of the applied magnetic field. In that figure, the maximum and minimum strain were not located at the 90°, 180°, and 270°: there was an approximately 10° shift toward larger angles, which is also the direction of the field rotation (CCW). This indicates the existence of hysteresis. Examining the third quadrant (190° to 280° of the field angle), the specimen was at its shortest length when the field angle was approximately 190°, because of the combined effects of the compressive stress and the transverse field favored the variant with its short axis parallel to the loading direction. When the field rotated away from 190°, the component of the field in the transverse direction decreased and the component of the field in the longitudinal direction increased. As result, the specimen started to lengthen. When the field reached 225°, approximately 2/3 of the ferromagnetic strain has been achieved, and the remaining 1/3 of ferromagnetic strain was achieved during the rest of the 45° of this quadrant. In other words, the changes in strain occurred faster in the first 45° of rotation than it did in the second 45° of the field rotation.

The surfaces of the specimens were observed optically during the experiments using a microscope equipped with DIC that allows the surface relief to be observed in false color. The images in Figure 7 were taken when the field was 5500 G in [001] and [$\bar{1}$00] directions. The strains were −0.013 and

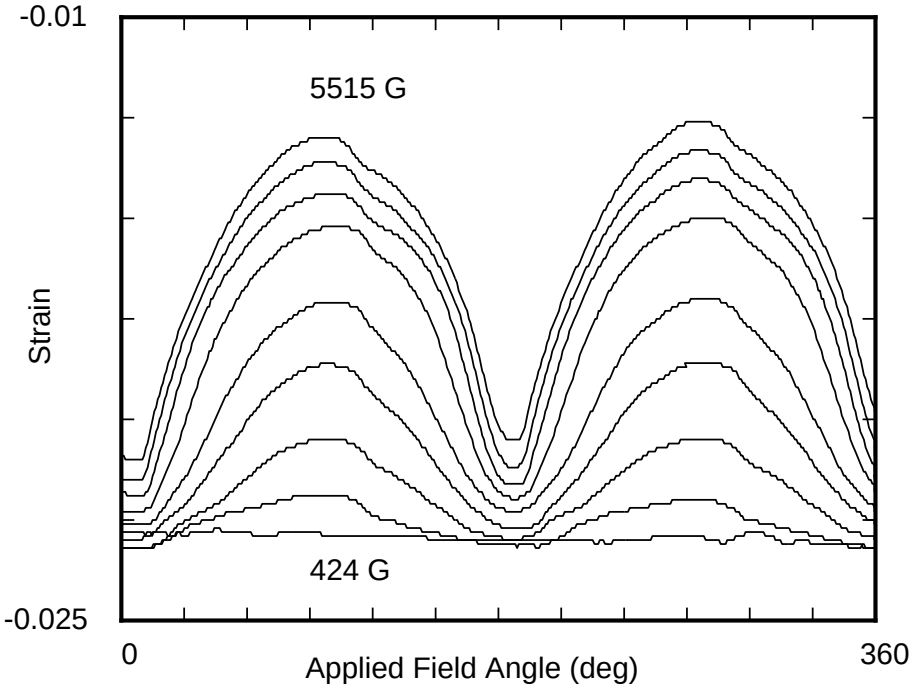

Figure 6. Strain vs. magnetic field rotation angle for test T5 at −1 MPa on specimen MM6.

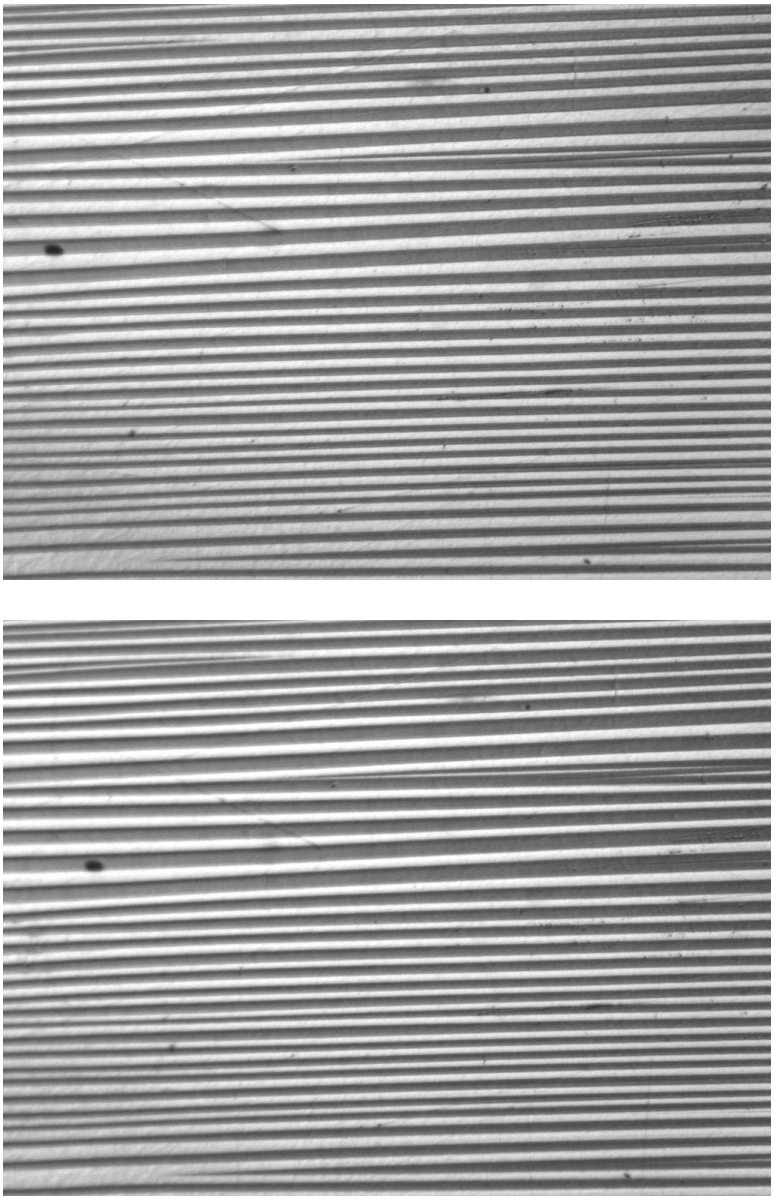

Figure 7. Microstructures of specimen MM6 when magnetic field is 5515 G in [001] (top) and in [$\bar{1}$00] (bottom). The images are from test T5 at −1 MPa and the field of view is approximately 0.3 mm wide. In these images the vertical [001] direction is up and the transverse [100] direction is horizontal.

−0.020. The strain difference between these two states is 0.007, which is about 14% of the theoretical ferromagnetic strain of 0.0515. However, comparison of these two images shows no clear differences. When the images are alternated on a computer screen a few small differences are visible in the thickness

Test	Temperature (°C)	Ferromagnetic Strain
T13b	20	0.0048
T13c	15	0.0071
T13d	10	0.0065
T14a	5	0.0069
T14b	0	0.0071
T14c	−5	0.0076

Table 5. Ferromagnetic strain amplitudes measured at various temperatures and under −1 MPa of stress for specimen MM6.

and configuration of the E_1/E_3 twin bands. The fact that the measured strain is so much smaller than that predicted from lattice parameters is the primary unresolved issue about the behavior of $Fe_{70}Pd_{30}$.

To assess the variation in the ferromagnetic strain amplitude with temperature, a series of measurements of the ferromagnetic strain at the various temperatures was conducted. The results of tests T13b-d and T14a-c (see Table 3 for test descriptions) are given in Table 5. These results show that the ferromagnetic strain does not depend on temperature, once the phase transformation is complete. Test T13b at 20°C is the temperature at which the martensite transformation begins, so at this temperature there is still a significant amount of austenite in the specimen. This accounts for the decreased strain amplitude measured in this test. The phase transformation is complete by 16°C and all experiments below this temperature have essentially the same strain amplitude.

5.2. ***Effects of initial microstructures and loading paths.*** The ferromagnetic shape-memory effect relies on the ability of the magnetic field to rearrange the martensitic variants. Thus the microstructure in the material plays a crucial role in the FSM behavior of the material. If the microstructure is arranged in such a way as to make twin boundary motion easy then the FSM behavior will be enhanced. On the other hand, if a complicated microstructure forms on cooling that does not easily lend itself to field-induced boundary motion, the FSM behavior may be adversely affected. Thus experiments were designed to attempt to generate different microstructures on cooling and compare their responses to applied fields. In addition, different field paths between identical field values where also used to assess the dependence of the FSM effect on the actuation path.

The amount of compressive stress applied to the specimen can be visually observed to affect the microstructure that forms on cooling. Small amounts of compressive stress allow microstructures with vertical twin bands (E_2/E_3 twins) to form, and in some cases remain, in the specimen during transformation. Larger values of compressive stress cause the transformation to form only horizontal twin bands (E_1/E_3 twins, such as those in Figure 7). Test T12 involved cooling the specimen under −12 MPa of stress to 11°C and then reducing the applied stress to −1 MPa before the magnetic field path Rot20-5515 was performed. Test T16 was cooled under −1 MPa of stress and then the same field path was performed. Figure 8 compares the strain responses during the first cycle of each of these tests. The results from T12 are at consistently larger (compressive) strain values, which is as expected due to the microstructural bias

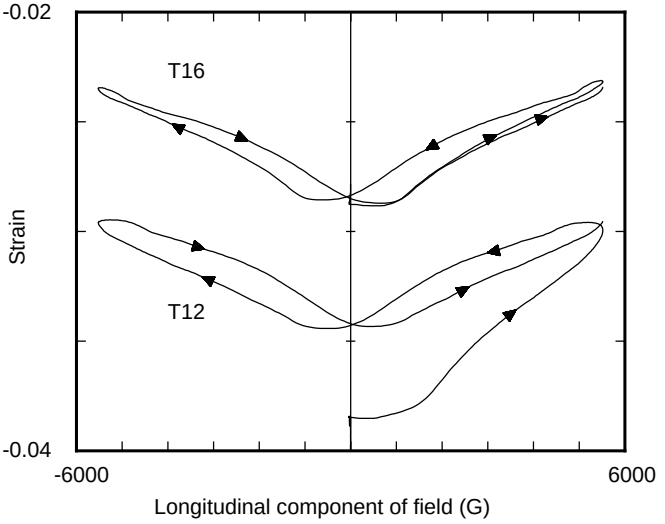

Figure 8. Strain versus field from tests T12 and T16 at −1 MPa and 11°C for specimen MM6 are shown. Test T12 included a bias stress of −12 MPa during the phase transformation, while test T16 had a bias stress of −1 MPa during cooling.

applied by the −12 MPa under which T12 cooled. A large fraction of this extra compressive strain is recovered on the application of the longitudinal field, which favors lengthening of the specimen, however, this recovery does not reverse on the removal of the field and the amplitude of the cyclic strain change is very similar in both tests. Ignoring the first 90° of field change when the irreversible recovery occurs, the average strain amplitude over the rest of the data shown in the figure is 0.0049 in test T12, and 0.0057 in test T16. It should be noted that the specimen is not fully detwinned by the −12 MPa stress, a small number of thin twin bands are still visible on the specimen surface after cooling is complete. When the stress is reduced to −1 MPa the bands become thicker and more numerous.

To study the effects of the field path, the paths Lin-4242 and Arc-4242 were designed. The results from two of the tests using these paths are shown in Figure 9. The strain verses longitudinal field component behavior is almost identical for the two tests. The large difference in the strain verses transverse field component plots is due to the fact that the arc path also has a longitudinal component to the field that grows as the transverse component is reduced. The solid circle and square symbols mark corresponding points on the arc path curves in both plots. This growing longitudinal component causes the specimen to lengthen on the arc path while the linear path causes no lengthening with its purely transverse field. The numerical values of the strain amplitudes for tests T2, T3, and T4 are given in Table 6. These data show that there is essentially no difference in the amplitudes measured for these two different field paths at the two different stress levels considered.

5.3. ***Comparison with constrained theory.*** Test T5 with a compressive stress of −1 MPa was selected for comparison with the results of the micromagnetic theory. As shown in Figure 10, there is a large discrepancy in the magnitude of the ferromagnetic strain predicted by theory and the experimental measurements. The theory predicts a ferromagnetic strain amplitude of 0.0515 compared to a measured

Test	Stress (MPa)	Ferromagnetic Strain Lin-4242	Arc-4242
T2	−2	0.0076	0.0074
T2	−1	0.0098	0.0090
T3	−2	0.0074	0.0068
T3	−1	0.0099	0.0090
T4	−2	0.0078	0.0068
T4	−1	0.0095	0.0085

Table 6. Ferromagnetic strain amplitudes measured in the tests T2, T3, and T4 at 11°C on specimen MM6.

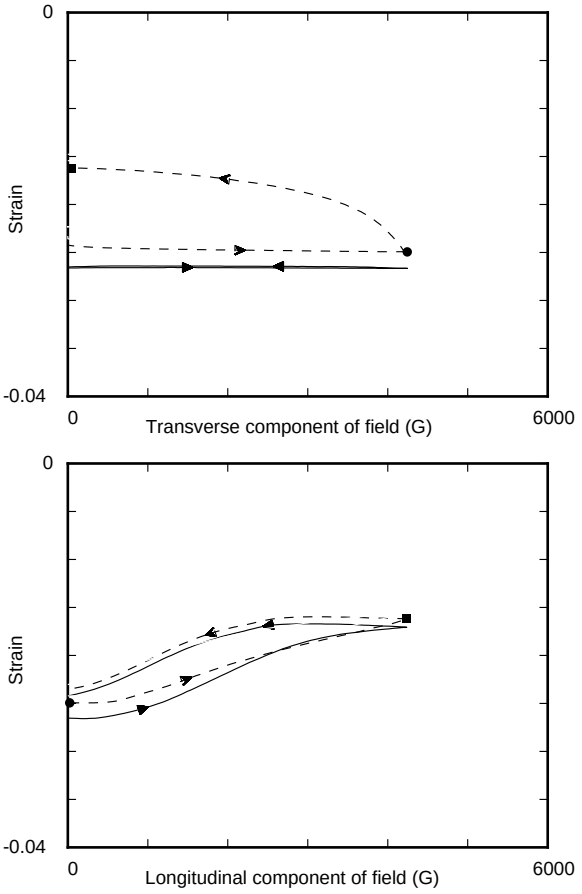

Figure 9. Strain versus field of test T3 at −1 MPa for specimen MM6. Dashed lines represent the strain response of the specimen when the field path is the arc rotation, and solid lines represent those with linear path. The dot and square indicate corresponding points on the two curves from the arc path.

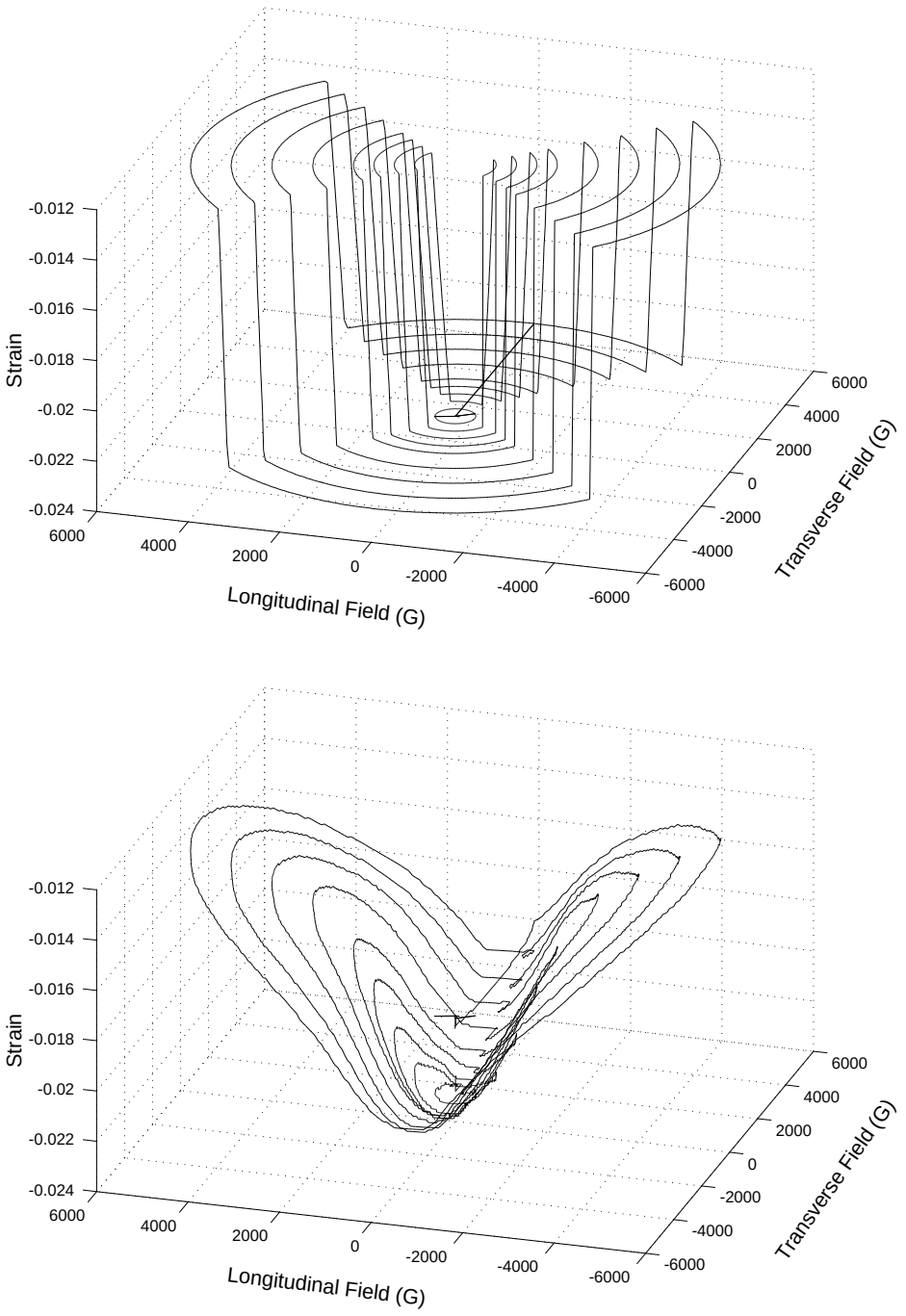

Figure 10. Comparison of the theoretical (top) and the experimental (bottom) results for field-induced strain of specimen MM6 at -1 MPa and 10°C. The total field-induced strain in top figure is scaled to 1/5 of the theoretical prediction.

value of 0.007. The basic shapes of the two sets of curves are similar and the constrained theory cannot be expected to capture smooth transitions between states that must occur due to the presence of microstructure and demagnetization. Because the theory assumed an infinite specimen, the finite nonellipsoidal shape of the specimen and its effects on the M-H curves were ignored. These effects give the M-H curves its gradual transition to saturation and will similarly affect the strain-field behavior of the specimen. Nonetheless, the curves do show a relative flat minimum when the magnitude of the longitudinal field is less than 440 G, and a tendency to flatten at higher fields. The sign of the strain changes agrees with the theory and this confirms that the long axis of the FCT martensite is the easy axis, otherwise a longitudinal field would make the specimen shorten. In addition, deviations from constrained theory are quite possible due to the finite values of the elastic moduli and magnetic anisotropy of the material. The magnetic anisotropy of $Fe_{70}Pd_{30}$ was found to be an order of magnitude smaller than that of Ni_2MnGa [Cui et al. 2004]. This small anisotropy means that it may be energetically less costly for the magnetization to rotate away from the easy directions in the material compared to moving a twin boundary that would result in a change in strain. This may be the reason for the small amount of ferromagnetic strain measured in this material.

6. Conclusions

The results presented above confirm that $Fe_{70}Pd_{30}$ is a FSM material and that its behavior agrees qualitatively with the predictions of the constrained theory for FSM materials. However, there are two results that are unexplained. The first is the small amount of ferromagnetic strain amplitude measured in this material. As just discussed in the previous paragraph, this may be due to the small magnetic anisotropy of this material. However, there are also a couple of unusual aspects to the shape-memory behavior of this material that may also contribute to the small strain amplitude. Observations of the microstructure that forms when this material is cooled through the transformation temperature are quite different from what is typically observed in shape memory materials (compared say to CuAlNi). Instead of a sharp planar austenite-martensite (A-M) interface with finely twinned martensite, the martensite in $Fe_{70}Pd_{30}$ grows into the austenite in a disorderly fashion. The predominate microstructure with a small volume fraction of martensite is a horizontal needle that appears to consist of a pair of martensite variants with a twin boundary down its middle. These needles grow into the austenite and then merge to give the final twinned martensite structure when the transformation is complete. Often the tips of these needles are arranged along what appears to be a roughly 45° line (the crystallographic theory of martensite predicts an A-M interface at nearly 45° with horizontal martensite twin interfaces) and they sometimes appear to move in unison, but this is far from the distinct A-M interface typically observed in shape memory materials. This type of behavior may indicate the $Fe_{70}Pd_{30}$ deviates substantially from the constrained theory. Because this transformation behavior is solely shape-memory related, this would indicate that the deviation is related to the elastic behavior of the material. Thus, elastic deformations may play an important role in the microstructure formation. Without accurate predictions of the microstructures in FSM materials, it will be very difficult to predict their behavior.

The second unusual aspect of the behavior of $Fe_{70}Pd_{30}$ involves its behavior in the martensitic state. When cooled under a stress of -12 MPa there are still some horizontal twin bands visible on the specimen surface when cooling is complete. Typical shape-memory materials would be completely detwinned by

this stress once the transformation was complete. Even more interesting, is that when the stress is reduced to -1 MPa from the -12 MPa applied during cooling (see the results for test T12) some twin boundary motion occurs. The twin bands thicken and the specimen lengthens. It is not known what force could be driving twin boundary motion that would grow the variants with their a axes in the compression direction at the expense of the variant with its shorter c axis in this direction when the amount of compressive stress is reduced. A typical shape memory material would not retwin until the stress became tensile. If there is some unknown microstructure related driving force in this material, the applied magnetic field would have to overcome this force to cause the FSM effect thus reducing the amount of strain achieved. Because there are only three tetragonal variants, it may be that there is a fair amount of elastic strain near the ends of specimen because of the lack of enough microstructural degrees of freedom to form a stress free microstructure there. These elastic strains could provide the energy needed for this type of behavior.

The second unexplained aspect of the behavior of $Fe_{70}Pd_{30}$ is the apparent lack of a blocking stress. Figure 4 shows that while the strain amplitude decays with increasing applied compressive stress, it is not decaying fast enough for the work output to decay as well. The results at -12 MPa are particularly notable. Aside from this data point, the work output does appear to have reached a maximum at approximately -4 MPa and is beginning to decrease. Because the strains measured at -12 MPa are the smallest, the relative error in this measurement will be the largest. If the strain was only 25% less than the reported value, the decreasing trend in the work output would continue to this stress level as well. The results reported in Figure 4 are from specimen MM10 using the capacitive sensor to measure the displacements. A constant bias or calibration error in this measurement would not effect the trends in the data. Additionally, the measurements are made under a constant stress so any elastic displacements of the compression fixture should cancel out in the amplitude calculation. Strain gauges are difficult to use on these materials, because they tend to debond during the phase transformation due to the large strains involved.

Future work on this material will focus on answering these questions. Measurement of the average magnetization of the material during testing will allow the possibility of magnetization rotation away from the easy axes to be assessed. In addition the shape-memory behavior will be studied further to provide a better understanding of the types of behaviors that have just been discussed. Finally, improvements to the constrained theory, such as including the specimen geometry, and the possibility of including deviations from constrained theory will be considered.

References

[Clark 1980] A. Clark, *Ferromagnetic materials*, North-Holland, Amsterdam, 1980.

[Cui and James 2001] J. Cui and R. D. James, "Study of Fe_3Pd and related alloys for ferromagnetic shape memory", *IEEE Trans. Magn.* **37**:4 (Part 1) (2001), 2675–2677.

[Cui et al. 2004] J. Cui, T. W. Shield, and R. D. James, "Phase transformation and magnetic anisotropy of an iron-palladium ferromagnetic shape-memory alloy", *Acta Mater.* **52**:1 (2004), 35–47.

[Cui et al. $\geq$ 2008] J. Cui, T. W. Shield, and R. D. James, "Effects of stress and magnetic field on the phase transformation in iron-palladium ferromagnetic shape memory alloys". In preparation.

[DeSimone and James 2002] A. DeSimone and R. D. James, "A constrained theory of magnetoelasticity", *J. Mech. Phys. Solids* **50**:2 (2002), 283–320.

[James and Kinderlehrer 1993] R. D. James and D. Kinderlehrer, "Theory of magnetostriction with applications to $Tb_xDy_{1-x}Fe_2$", *Philos. Mag. B* **68** (1993), 237–274.

[James and Wuttig 1998] R. D. James and M. Wuttig, "Magnetostriction of martensite", *Philos. Mag. A* **77**:5 (1998), 1273–1299.

[Muto et al. 1988] S. Muto, S. Takeda, R. Oshima, and F. E. Fujita, "High resolution electron microscopy of the tweed microstructure in an Iron-Palladium alloy", *Jpn. J. Appl. Phys. 2* **27**:8 (1988), 1387–1389.

[Muto et al. 1990a] S. Muto, R. Oshima, and F. E. Fujita, "Consideration of the tweed structure of Fe-Pd alloys by continuum elasticity theory", pp. 65–70 in *Martensitic transformations: proceedings of the 6th International Conference* (Sydney, 1989), vol. 1, edited by B. C. Muddle, Materials Science Forum **56**, Trans Tech Publications, Aedermannsdorf, Switzerland, and Brookfield, VT, 1990.

[Muto et al. 1990b] S. Muto, S. Takeda, and R. Oshima, "Analysis of lattice modulations in the tweed structure of an Fe-Pd alloy by image processing of a high resolution electron micrograph", *Jpn. J. Appl. Phys. 1* **29**:10 (1990), 2066–2071.

[Muto et al. 1990c] S. Muto, S. Takeda, R. Oshima, and F. E. Fujita, "High resolution electron microscopy of tweed microstructure in Fe-Pd alloys", pp. 45–50 in *Martensitic transformations: proceedings of the 6th International Conference* (Sydney, 1989), vol. 1, edited by B. C. Muddle, Materials Science Forum **56**, Trans Tech Publications, Aedermannsdorf, Switzerland, and Brookfield, VT, 1990.

[O'Handley 1998] R. C. O'Handley, "Model for strain and magnetization in magnetic shape-memory alloys", *J. Appl. Phys.* **83**:6 (1998), 3263–3270.

[Oshima 1981] R. Oshima, "Successive martensitic transformations in Fe-Pd alloys", *Scr. Metall.* **15**:8 (1981), 829–833.

[Oshima and Sugiyama 1982] R. Oshima and M. Sugiyama, "Martensite transformations in iron-palladium alloys", *J. Phys.* (*Paris*) *Colloq.* **43**:C4 (1982), 383.

[Oshima et al. 1988] R. Oshima, M. Sugiyama, and F. E. Fujita, "Tweed structures associated with FCC-FCT transformations in Fe-Pd alloys", *Metall. Trans. A* **19**:4 (1988), 803–810.

[Oshima et al. 1990] R. Oshima, K. Tanaka, A. Taniyama, and F. E. Fujita, "Study of BCT martensite of Fe-Pd alloys", pp. 175–180 in *Martensitic transformations: proceedings of the 6th International Conference* (Sydney, 1989), vol. 1, edited by B. C. Muddle, Materials Science Forum **56**, Trans Tech Publications, Aedermannsdorf, Switzerland, and Brookfield, VT, 1990.

[Oshima et al. 1992] R. Oshima, S. Muto, and F. E. Fujita, "Initiation of FCC-FCT thermoelastic martensite transformation from premartensitic state of Fe-30 at Pd alloys", *Mater. Trans.* (*JIM*) **33**:3 (1992), 197–202.

[Shield 2003] T. W. Shield, "A magnetomechanical testing machine for ferromagnetic shape-memory alloys", *Rev. Sci. Instrum.* **74**:9 (2003), 4077–4088.

[Somura and Oshima and Fujita 1980] T. Sohmura, R. Oshima, and F. E. Fujita, "Thermoelastic FCC-FCT martensitic transformation in Fe-Pd alloy", *Scr. Metall.* **14**:8 (1980), 855–856.

[Sozinov et al. 2002] A. Sozinov, A. A. Likhachev, and K. Ullakko, "Crystal structures and magnetic anisotropy properties of Ni-Mn-Ga martensitic phases with giant magnetic-field-induced strain", *IEEE Trans. Magn.* **38**:5 (Part 1) (2002), 2814–2816.

[Sugiyama et al. 1984] M. Sugiyama, R. Oshima, and F. E. Fujita, "Martensitic transformation in the Fe-Pd alloy system", *Trans. Jpn. Inst. Met.* **25**:9 (1984), 585–592.

[Sugiyama et al. 1985] M. Sugiyama, S. Harada, and R. Oshima, "Change in Young's modulus of thermoelastic martensite Fe-Pd alloys", *Scr. Metall.* **19**:3 (1985), 315–317.

[Sugiyama et al. 1986] M. Sugiyama, R. Oshima, and F. E. Fujita, "Mechanism of FCC-FCT thermoelastic martensite transformation in Fe-Pd alloys", *Trans. Jpn. Inst. Met.* **27**:10 (1986), 719–730.

[Tanaka and Oshima 1991] K. Tanaka and R. Oshima, "Role of annealing twin in the formation of variant structure of Bct martensite in Fe-Pd alloy", *Mater. Trans.* (*JIM*) **32**:4 (1991), 325–330.

[Tanaka et al. 1992] K. Tanaka, K. Hiraga, and R. Oshima, "Origin of tetragonality of BCT martensite in substitutional Fe-Pd(-Ni) disordered alloys", *Mater. Trans.* (*JIM*) **33**:3 (1992), 215–219.

[Tickle and James 1999] R. Tickle and R. D. James, "Magnetic and magnetomechanical properties of Ni_2MnGa", *J. Magn. Magn. Mater.* **195**:3 (1999), 627–638.

[Tickle et al. 1999] R. Tickle, R. D. James, T. W. Shield, M. Wuttig, and V. V. Kokorin, "Ferromagnetic shape memory in the NiMnGa system", *IEEE Trans. Magn.* **35**:5 (Part 3) (1999), 4301–4310.

[Ullakko et al. 1996] K. Ullakko, J. K. Huang, C. Kantner, R. C. O'Handley, and V. V. Kokorin, "Large magnetic-field-induced strains in Ni_2MnGa single crystals", *Appl. Phys. Lett.* **69**:13 (1996), 1966–1968.

[Vasil'ev et al. 1996] A. N. Vasil'ev, S. A. Klestov, R. Z. Levitin, and V. V. Snegirev, "Magnetoelastic interaction in the martensitic transformation in an Ni_2MnGa single crystal", *J. Exp. Theor. Phys.* **82**:3 (1996), 524–526.

Received 29 Dec 2005. Accepted 18 Sep 2006.

JUN CUI: cui@research.ge.com
GE Global Research Center, K1-2D47, One Research Circle, Niskayuna, NY 12302, United States

TOM SHIELD: shield@aem.umn.edu
Department of Aerospace Engineering and Mechanics, University of Minnesota, 107 Akerman Hall, 110 Union St. SE, Minneapolis, MN 55455, United States